Tuning the size of poly(butylene oxide) nanoparticles by microfluidic-assisted nanoprecipitation

Lachlan Alexander, Marat Mamurov, Hiba Khelifa, Nicolas Illy, Philippe Guégan, Christophe M Thomas, Samuel Hidalgo-Caballero, Joshua D Mcgraw, Kawthar Bouchemal

Tuning the size of poly(butylene oxide) nanoparticles by microfluidic-assisted nanoprecipitation

Lachlan Alexander,[a,b,c#] Marat Mamurov,[a,c#] Hiba Khelifa,[a,d#] Nicolas Illy,[d] Philippe Guégan,[d] Christophe M. Thomas,[a] Samuel Hidalgo-Caballero,[c,e] Joshua D. McGraw,[c,e*] and Kawthar Bouchemal [a*]

a. Chimie ParisTech, PSL University, CNRS, Institut de Recherche de Chimie Paris, 75005 Paris, France.

b. Monash University, Clayton, Australia.

c. Gulliver, CNRS, ESPCI Paris, Université PSL, 75005 Paris, France

d. Sorbonne Université, CNRS, Institut Parisien de Chimie Moléculaire, IPCM, F-75005 Paris, France

e. Institut Pierre Gilles de Gennes (IPGG), ESPCI Paris, Université PSL, 75005 Paris, France

[#] Equally contributing first authors

* Corresponding authors

kawthar.bouchemal@chimieparistech.psl.eu

joshua.mcgraw@espci.fr

Abstract

Microfluidic-assisted nanoprecipitation provides precise control over formulation conditions, enabling for the design of nanoparticles with highly tunable properties. This study explores the influence of channel geometry, flow dynamics, and polymer concentration on the size and polydispersity of poly(butylene oxide) (PBO) nanoparticles. PBO is a hydrophobic polymer with a low glass transition temperature (T_g = –71 °C) that typically forms large nanoparticles (>176 nm) via bulk nanoprecipitation, as well as aggregates ranging from 3000–5000 nm. Using a hydrodynamic flow-focusing Ψ-geometry, we demonstrate that higher total flow rates increase convective mixing, reduce mixing times, and produce smaller, more monodisperse PBO nanoparticles. A comparative analysis of Ψ- and T-channel geometries across various dimensions revealed that Ψ-geometries consistently outperformed T-geometries due to their superior mixing efficiency. Decreasing the channel dimensions to 20 µm further improved mixing by shortening diffusion lengths and accelerating solvent–antisolvent interdiffusion. Using the Ψ-geometry, nanoparticles as small as 66 nm were achieved, whereas T-geometries produced significantly larger particles (>500 nm). A linear trend between particle size and total flow was observed, best described by a power-law relationship, linking flow rate—and by extension, Reynolds number—to mixing speed and nanoparticle size. These findings highlight the pivotal role of microfluidic design and flow control in tailoring nanoprecipitation for low-T_g, hydrophobic polymers such as PBO. This approach shows promising potential for the encapsulation and delivery of hydrophobic drugs.

Keywords: Polybutylene oxide; Nanoprecipitation; Microfluidics; Hydrodynamic flow-focusing; Low glass transition polymers; Nanoparticle formulation.

1. Introduction

Nanoprecipitation—also referred to as solvent displacement or flash precipitation—is a simple yet versatile technique for producing polymeric nanoparticles with applications in drug delivery and diagnostics.[1] It was first introduced by Fessi et al.[2, 3] It involves the rapid mixing of a polymer-containing organic solvent with an aqueous non-solvent, resulting in a sudden decrease in polymer solubility, nucleation, and nanoparticle formation.[4] Surfactants are often added to stabilize the resulting colloidal suspension and to prevent aggregation, while the inclusion of active pharmaceutical ingredients in the organic phase allows for the co-formation of drug-loaded nanoparticles.[5]

The efficiency and outcome of nanoprecipitation depend strongly on several parameters, including solvent–non–solvent miscibility[6], surfactant concentration, polymer concentration,[7] and most critically, the dynamics of mixing.[8] In conventional bulk nanoprecipitation (Fig. 1a), the organic phase is typically introduced into the aqueous phase under continuous stirring. However, this method has low reproducibility, broad particle size distributions, and limited control over nucleation and growth. Moreover, turbulent mixing regimes—achieved through devices such as T-mixers or Y-mixers—have been explored to reduce particle size [8-10], but even under high Reynolds number conditions ($Re \approx 12{,}000$), the smallest particle sizes obtained were around 185 nm.[9] These limitations hinder the development of nanoparticles in the sub-100 nm range. The small size of nanoparticles, less than 100 nm, makes them similar to physiological molecules and may enable them to use the same entry mechanisms across internal barriers.[11, 12]

To overcome the inherent limitations of bulk nanoprecipitation, microfluidic-assisted nanoprecipitation has emerged as a promising alternative. By confining fluid flow to microchannels, microfluidics enables precise control of mixing parameters such as total flow rate, flow ratio, and channel geometry. This leads to improved reproducibility and narrower particle size distributions.[13, 14] Even under laminar flow regimes, efficient mixing can be achieved through hydrodynamic flow focusing and geometrically optimized micromixers.[15-18] The effectiveness of this approach is often

quantified through parameters such as mixing time (τ_{mix}), Reynolds number, and interdiffusion length. These parameters can be tuned via device design.[16, 19]

Despite the progress in microfluidic nanoprecipitation, most studies have focused on polymers with relatively high glass transition temperatures (T_g), such as polylactic acid (PLA, $T_g \approx 60$–65 °C), or on amphiphilic copolymers like PLA-polyethylene glycol and poly(lactic-*co*-glycolic acid).[15] These polymers offer greater structural rigidity, which facilitates nanoparticle formation. In contrast, highly hydrophobic homopolymers with low T_g remain underexplored. Their inherent mobility and propensity to aggregate in aqueous environments pose significant formulation challenges.

In this context, poly(butylene oxide) (PBO) represents a particularly challenging and understudied candidate. PBO is a flexible, hydrophobic polyether with a very low T_g of –73 °C.[20] At room temperature, it exists in a viscous, amorphous state, which greatly limits its processability via conventional methods. Consequently, PBO has been used primarily in block copolymers with hydrophilic segments like polyethylene oxide or polyglycidol to facilitate self-assembly into micelles or vesicles.[21] To our knowledge, no prior study has reported the successful direct nanoprecipitation of pure PBO homopolymer into stable nanoparticles.

This study addresses the existing gap in the literature by demonstrating—for the first time—the microfluidic-assisted nanoprecipitation of pure PBO. Using Ψ-geometry microfluidic devices, we enhanced mixing via hydrodynamic flow focusing. We also show how tuning adjusting flow conditions and channel dimensions can overcome PBO's intrinsic limitations. By systematically varying the flow ratio, total flow, and channel geometry, we reveal how mixing efficiency influences the nucleation and growth of PBO nanoparticles. Interestingly, we produced monodisperse PBO nanoparticles as small as 66 nm, which is far below the limits of traditional bulk techniques. This advance not only establishes a scalable process for an otherwise intractable polymer and provides broader insights into designing formulations of low-T_g, hydrophobic homopolymers using microfluidic systems. Our findings contribute to a growing body of work focused on expanding the materials

compatibility in microfluidic nanoprecipitation, which has implications for the delivery of hydrophobic drugs and the engineering of novel nanocarriers.

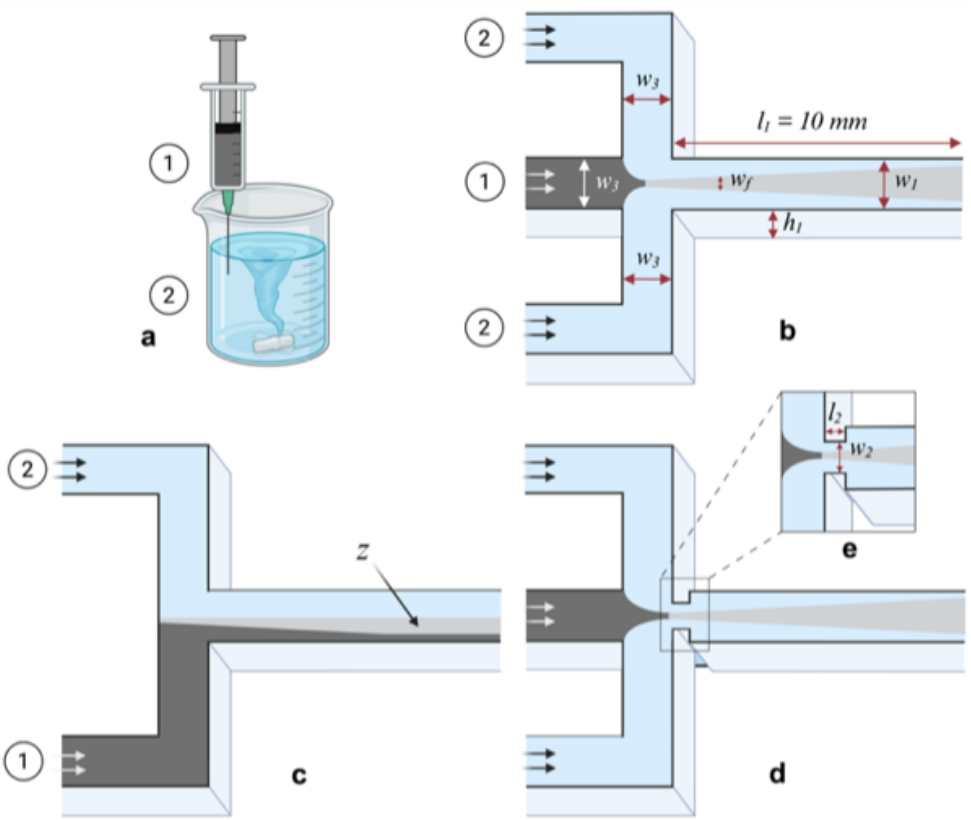

f

Chip channel dimensions for T, ψ and ψ_J-geometry			Dimensions of the junction for ψ_J-geometry		
w_1 (μm)	h_1 (μm)	$A_{Channel}$ (10^2 μm²)	w_2 (μm)	l_2 (μm)	A_J (10^2 μm²)
100	100	100	20	30	20
40	40	16	8	12	3.2
20	20	4	4	6	0.8

Fig. 1. Schematic representation of bulk nanoprecipitation (a) and in a microfluidic-assisted device (b,c,d). Different geometries were used for microfluidic devices: Ψ-geometry without junction (b), T geometry (c), and Ψ_J-geometry with a junction (d). Dimensions of the channel chips and J-geometry junction (detailed in e) are indicated in (f). The channel length (l_1) and the channel width before mixing (w_3) were kept constant (l_1 = 10 mm and w_3 = 75 μm). (1) aqueous phase, (2) organic phase. The light grey region (*z*) represents the interdiffusion zone. A represents the cross sections of the channel ($A_{Channel}$) or the junction (A_J).

2. Experimental section

2.1. Materials

Benzyl alcohol (BA, anhydrous, 99.8%, (1) in **Scheme 1**), phosphazene base *t*BuP4 (1-tert-butyl-4,4,4-tris(dimethylamino)-2,2-bis[tris(dimethylamino)-phosphoranylidenamino] 2λ5,4λ5-catena

di(phosphazene)) (0.8 mol L^{-1} in n-hexane, (2) in **Scheme 1**), aluminum oxide, *N*,*N*-dimethylformamide (DMF), butylene oxide (BO, (3) in **Scheme 1**), HCl, $NaHCO_3$, calcium hydride (CaH_2, ca. 93%), deuterated chloroform ($CDCl_3$), surfactants (Tween® 80, Span® 80), and phosphotungstic acid (contrast agent for TEM observations) were purchased from Sigma-Aldrich (St. Quentin Fallavier, France). Lithium bromide (LiBr), dichloromethane (DCM), methanol, tetrahydrofuran, ethanol (>99.5%), and toluene were purchased from VWR Chemical (Pessac, France).

Noteworthy, BA and *t*BuP4 were stored in a glovebox until use. The monomer BO was dried twice over calcium hydride by cryo-distillation and was then stored in a glovebox. A solvent purification system (MBraun SPS-800, Garching, Germany) was used to dry toluene and THF under nitrogen.

Polytetrafluoroethylene (PTFE) filters with a porosity of 0.22 µm were purchased from Merck (Guyancourt, France). Size exclusion chromatography (SEC) columns and poly(methyl methacrylate) (PMMA) standards were purchased from Polymer Standard Services (Agilent Technologies, Les Ulis, France). Glovebox (MBraun Labstar, Garching, Germany) has a purification system and a dry nitrogen atmosphere.

Milli-Q® water was used for all the experiments (Resistivity 18.2 MΩ.cm at 21 °C, Millipore purification system, Millex, SLAP 0225, Millipore, France). Ethanol and water were filtered through a 0.45 µm filter before use.

The density and the viscosity of the aqueous and the organic as well as PBO nanoparticle suspension were determined as detailed in the Supporting Information (Table S1, S2, and Fig. S1).

2.2. Methods

2.2.1. PBO synthesis and characterization

2.2.1.1. PBO Synthesis

The PBO was synthesized in a glovebox according to the procedure reported by Illy *et al* (**Scheme 1**).[22] Typically, BO (957 µL, 11 mmol, 87 eq.) was introduced into a 100 mL single-chambered

glass flask (Lenz Laborglasinstrumente™ 03002970). Then, 1 mL of toluene was introduced under nitrogen, followed by BA (13 µL, 0.126 mmol, 1 eq.), and *t*BuP4 solution (125 µL, 0.1 mmol, 1 eq.). Notably, *t*BuP4 and BA were added using a microsyringe (Hamilton Company, reference 87930), while toluene (1 mL) was added using a plastic syringe (B. Braun, reference 720-2561). After closure of the flask, the reaction was stirred at 25 °C for 24 h. An aliquot was collected from the polymerization tube and analyzed by ^{1}H NMR. A complete conversion of the monomer corresponds to the disappearance of the triplet at 2.7 ppm assigned to the monomer's epoxide ring. After confirming the consumption of BO, a termination step was undergone by breaking the inert conditions. Subsequently, the solvent was removed by rotary evaporation. Then, the polymer was dissolved in DCM and purified by passing through neutral aluminum oxide to eliminate *t*BuP4. ^{1}H NMR in deuterated $CDCl_3$ confirmed the effectiveness of the purification. The solvent was removed by rotary evaporation under a vacuum at 50 °C, followed by drying overnight under vacuum to give a yellowish viscous liquid.

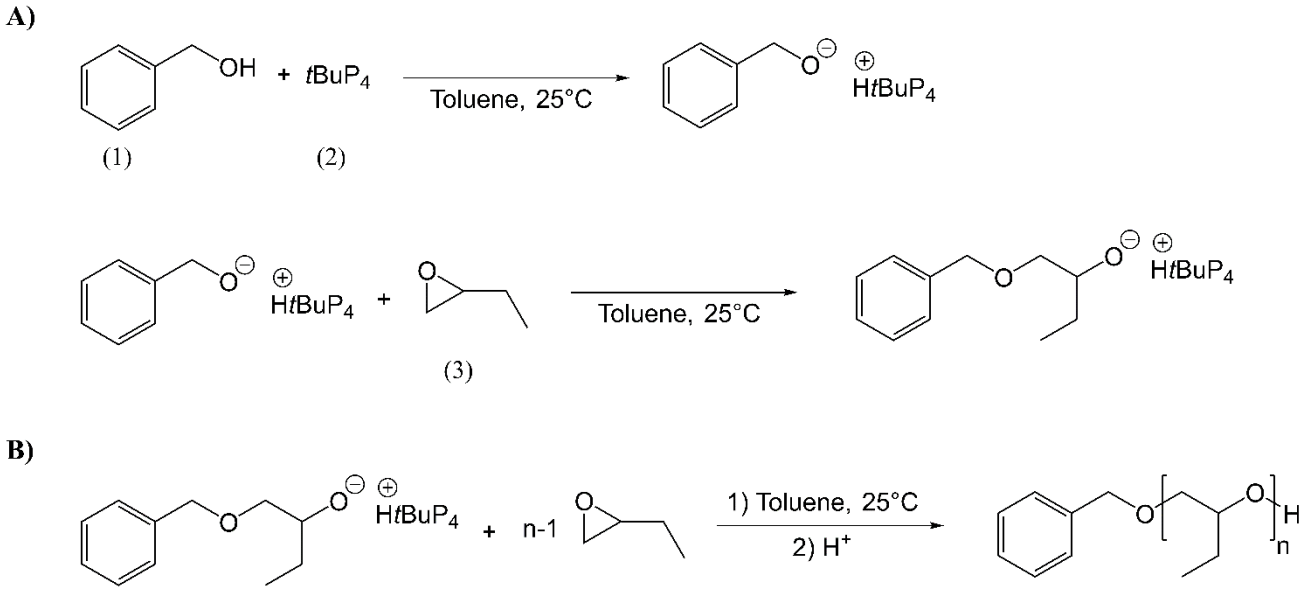

Scheme 1. Schematic representation of PBO polymerization. (1) corresponds to benzyl alcohol, (2) to phosphazene base *t*BuP4, and (3) to butylene oxide.

2.2.1.2. PBO characterization

PBO number-average molar mass was determined by ^{1}H NMR spectroscopy (denoted $M_{n(NMR)}$). PBO ^{1}H NMR spectra were recorded in $CDCl_3$ using a Bruker 300 MHz NMR spectrometer. The polymer concentration in the solution was 15 mg mL^{-1}.

Size exclusion chromatography (SEC) in THF was carried out on three PL gel Mixed-C 5 µm columns (7.5 ´ 300 mm; separation limits: 0.2 to 2 × 10^6 g mol^{-1}) maintained at 40 °C and coupled with a Viscotek GPCmax delivery module and two modular detectors: a Viscoteck 3580 differential refractive index detector and a Shimadzu SPD20-AV diode array UV detector. The mobile phase flow rate was 1.0 mL min^{-1}, and toluene was used as a flow rate marker. Samples were prepared by dissolving PBO in tetrahydrofuran at a 5 mg mL^{-1} concentration. After filtration through a 0.22 µm pore-size PTFE syringe filter, PBO solution was injected (50 µL). The OmniSEC 4.7 software was used for data acquisition and analysis in all cases. The number-average molar mass $M_{n(SEC)}$ and the dispersity $Đ$ of the PBO were calculated from poly(methyl methacrylate) standards using a differential refractive index detector.

PBO thermal behavior was evaluated by differential scanning calorimetry (DSC) using a TA DSC Q2000 device (Guyancourt, France) calibrated with an indium standard. The sample was placed in an aluminum capsule and initially cooled to -80 °C. Two cycles of heating (10 K min^{-1}) and cooling (10 K min^{-1}) were then applied in the temperature range of -80 to +130 °C. The samples' glass transition temperatures (T_g) were taken from the midpoint of the step in specific heat increments using the second heating cycle.

2.2.2. PBO nanoparticle preparation via bulk nanoprecipitation

Nanoprecipitation was performed to prepare PBO nanoparticles by adapting the protocol published by Bouchemal et al.[6] The organic phase was prepared by weighting in a small vial PBO (7.5 mg) and Span® 80 (2 mg), used as a lipophilic surfactant. Then, ethanol (1 mL) was added to the vial.[6]

The organic phase was homogenized by a magnetic stirring for a few minutes. The aqueous phase was prepared by weighting in a small vial Tween® 80 (6.8 mg), used as a hydrophilic surfactant. Then, water (2 mL) was added to the vial, followed by magnetic stirring until complete surfactant dissolution. The organic phase was then collected in a 2-mL plastic syringe (B Braun™ 4606027V) with an 18-G needle (Microlance 3) and then rapidly injected into the continuous phase under magnetic stirring (400 rpm at 25 °C) (Fig. 1a). The injection speed was 4 s for 1 mL of organic phase. The magnetic stirring is maintained for 30 min. The organic solvent was removed by evaporating overnight under a fume hood at room temperature.[6]

2.2.3. PBO nanoparticle preparation via microfluidic-assisted nanoprecipitation

2.2.3.1. Microfluidic chip fabrication

A commercial polydimethylsiloxane elastomer (PDMS, Momentive RT 615 A & B) was utilized for chip fabrication (Refer to Supporting Information for additional details). PDMS and the associated crosslinker were mixed in a 10:1 ratio and poured onto a lithography-etched aluminum mold containing the microfluidic design given in Fig. 1b-1f. The design was then placed in a vacuum chamber under vacuum until all air bubbles were removed, typically for one hour at room temperature. The design was then transferred to an oven at 70 ºC for 3 h, allowing the PDMS to solidify. The individual chips were then cut from the mold, placed into a plasma cleaner with a glass microscope slide, and exposed to oxygen plasma at 50 W for one minute. Once removed from the plasma chamber, the chip was pressed gently, with the design facing down, onto the glass slide to finalize the chip. Inlet and outlet holes were punched into the chip using a coring punch. During storage, scotch tape was placed over the chip to prevent exposure to dust.

2.2.3.2. Nanoparticle preparation by microfluidic-assisted nanoprecipitation

Nanoparticles were produced using a PDMS-based microfluidic chip connected to two 11 Pico Plus Elite Pump Module (Harvard Apparatus, Courtaboeuf, France), each loaded with 10 mL 100 Series gastight Hamilton syringes. The syringes were filled with the aqueous and polymer-containing organic

phases and connected via 0.5 mm inner diameter silicone tubing fitted with 23G stainless steel microfluidic adaptors. The organic phase was connected to the inner inlet of the PDMS chip, while the aqueous phase was connected to the outer inlet. The entire chip setup was mounted under a B-190TBPL microscope (Optika, Italy) for visual alignment and monitoring.

The syringe pumps were connected to a Pump Controller (Harvard Apparatus, Courtaboeuf, France), wherein the aqueous and organic phase flow rates were programmed to satisfy the experimental requirements, as explained in the next section.

Flow rates for the aqueous and organic phases were programmed via the connected pump controller to match the experimental design parameters detailed in the next section. The organic phase (ethanol containing PBO and Span 80) was injected at flow rates corresponding to an organic-to-aqueous phase flow ratio (R) of 0.06. PBO concentrations were varied at 1.87, 3.75, and 7.5 mg mL^{-1}, while the total flow rate ranged from 32 to 96 µL min^{-1}.

For each condition, the system was run long enough to collect 100 µL of nanoparticle suspension. To evaluate operational stability and reproducibility, each device was used for multiple successive runs over a continuous period of at least 60 min. During this time, no device fouling, clogging, or channel deformation was observed.

2.2.3.3. Investigation of the impact of process parameter variation on nanoparticle size

Microfluidic geometry and dimensions were modified, as detailed in Fig. 1b-1f. A microfluidic hydrodynamic flow-focusing (HFF) device was first explored (denoted as Ψ-geometry, Fig. 1b), and the results were compared to T-geometry (Fig. 1c); in order to limit the parameter variations, we confine ourselves in this study to the use of square-channel geometries. Then, the impact of the presence of a junction (J-type) on mixing behavior and nanoparticle size was explored (Fig. 1a). The results were compared to nanoparticle size obtained without junction (Ψ-type) (Fig. 2b) and T-type geometry (Fig. 2c).

2.2.3.4. Equations to calculate microfluidic parameters

The Reynolds numbers of the aqueous phase, the organic phase, and the nanoparticle suspension (denoted as Re_{Aq}, Re_{Org}, and Re_{mix}, respectively) were calculated according to Eq. (A.1), Eq. (A.2), and Eq. (A.3), respectively:

$$Re_{Aq} = \frac{u_{Aq} w_1}{\nu_{Aq}} \quad \text{Eq. (A. 1)}$$

$$Re_{Org} = \frac{u_{Org} w_1}{\nu_{Org}} \quad Eq. (A. 2)$$

$$Re_{mix} = \frac{u_{Mix} w_1}{\nu_{Mix}} \quad \text{Eq. (A. 3)}$$

Where ν_{Aq}, ν_{Org}, and ν_{mix} ($m^2\ s^{-1}$) are the kinematic viscosity of the aqueous phase, the organic phase before mixing, and the nanoparticle suspension after mixing; u_{Aq}, u_{Org}, and u_{mix} correspond to the jet velocity ($m\ s^{-1}$) of the aqueous phase and the organic phases before mixing ($m^2\ s^{-1}$); u_{mix} is the jet velocity of the nanoparticle suspension after mixing. u_{Aq}, u_{Org}, and u_{mix} were calculated according to Eq. (B. 1), Eq. (B. 2), and Eq. (B. 3), respectively.

$$u_{Aq} = Q_{Aq}/A_{Channel} \quad \text{Eq. (B. 1)}$$

$$u_{Org} = Q_{Org}/A_{Channel} \quad \text{Eq. (B. 2)}$$

$$u_{mix} = TF/A_{Channel} \quad \text{Eq. (B. 3)}$$

Where Q_{Aq} and Q_{Org} are the flow rates of the aqueous and the organic phases, respectively ($mm^3\ s^{-1}$). TF is the total flow ($mm^3\ s^{-1}$, the sum of Q_{Aq} and Q_{Org}), and $A_{Channel}$ is the microfluidic channel cross section (Fig. 1f).

Mixing time, τ_{mix} was calculated according to Eq. (C. 1).

$$\tau_{mix} \sim \frac{w_f^2}{4D} \approx \frac{w_1^2}{9D} \frac{1}{\left(1 + \frac{1}{R}\right)^2} \quad \text{Eq. (C. 1)}$$

Where D represents the diffusivity index of the solvent in water (for ethanol, $D = 1.22 \times 10^{-9}\ m^2\ s^{-1}$) and R is the flow ratio. It is calculated by dividing the flow of the organic phase (Q_{Org}) by the flow

of the aqueous phase (Q_{Aq}). w_f is the width of the focused stream (m) (Fig. 1b and 1c), and w_1 is the microfluidic channel width (m).

The residence time of the suspensions in the channel of the microfluidic device (τ_{res}, s) is calculated according to Eq. (D. 1).

$$\tau_{res} = l_1/u \quad \text{Eq. (D. 1)}$$

The mixing distance corresponding to the distance required for complete mixing (l_{mix}, m) is calculated according to Eq. (E. 1).

$$l_{mix} = u\tau_{mix} \quad \text{Eq. (E. 1)}$$

To estimate the aggregation time (τ_{agg}) in our study on the nanoprecipitation of PBO, we relied on principles derived from nucleation–aggregation kinetics reported by Karnic *et al*[14] and Johnson & Prud'homme.[23] In microfluidic systems under laminar flow, it is generally assumed that unimers (individual polymer chains) diffuse and aggregate following second-order kinetics. Under these conditions, the aggregation time can be estimated by Eq. (F1):

$$\tau_{agg} \sim \frac{1}{k\ C_p} \quad \text{Eq. (F1)}$$

Where: C_p is the polymer concentration in mol m^{-3} and k is the aggregation rate constant, typically defined in the diffusion-limited regime as Eq. (F2):

$$k = 4\pi D R_h \quad \text{Eq. (F2)}$$

Where R_h is the assumed radius of nucleus and D the diffusivity of PBO.

Thus, τ_{agg} can be calculated from Eq. (F3):

$$\tau_{agg} \sim \frac{1}{4\ D\ R_h\ C_p} \quad \text{Eq. (F3)}$$

2.3. Nanoparticle physicochemical characterization

2.3.1. Dynamic light scattering

The mean hydrodynamic diameters (d_h) of nanoparticles were measured by dynamic light scattering (DLS) using a Zetasizer Nanoseries. Bulk nanoprecipitation samples were prepared by diluting 2 µL of the sample in 1 mL water. Microfluidic samples were not diluted. Particle size was measured at 25 °C. The scattering angle was 173°. Each experiment was replicated three times on three independent formulations.

2.3.2. Zeta potential

The particle surface potentials were calculated from the electrophoretic mobility using an electrophoretic light-scattering technique (Zetasizer Nanoseries, Malvern Instruments, Ltd., UK). For sample preparation, 500 µL of each suspension was diluted with NaCl (1 mM) (500 µL). Dilution was optimized to reach an attenuation of 6. Then, 1 mL of each suspension was placed in a disposable folded capillary cell (DTS1070). Zeta potentials were measured at 25 °C.

2.3.3. Transmission electron microscopy

Transmission electron microscopy (TEM) characterizations were performed at 80 kV transmission using a transmission electron microscope (JEOL 1400) coupled to TEM Domain Centre software. Samples were prepared as detailed in our previous publication.[24] Typically, 1 µL suspensions were diluted in water (49 µL) and manually homogenized. Then, 4 µL suspensions were placed on a plasma-treated carbon grid for 40 seconds The samples were further stained with 2% (w/v) phosphotungstic acid for 40 seconds. After 5 min of drying at room temperature, the grid was placed on a slide and inserted into the microscope for observation.

2.4. Software

All ^{1}H NMR spectra were analyzed with Bruker Topspin software and referenced to residual proton peaks of deuterated solvent.

2.5. Statistical analyses

GraphPad prism® version 9.0 software was used for statistical analyses. A two-way Kruskal-Wallis test was applied, followed by a Tukey's multiple comparison post-test. The significance level for all statistical analyses was set at a p-value < 0.05.

3. Results

3.1. PBO synthesis and characterization

The PBO homopolymer was synthesized by anionic ring-opening polymerization using a benzyl alcohol-*t*BuP4 initiator (**Scheme 1**). Benzyl alcohol hydroxyl groups were deprotonated by the *t*BuP4 phosphazene base, forming highly reactive alkoxides that are associated with phosphazenium cations. These alkoxides initiated the polymerization of the BO monomers (Fig. 2a-c). The resulting PBO was passed through neutralized aluminum oxide. After this treatment, the ^{1}H NMR spectrum showed all the characteristic signals of both PBO and benzyl alcohol. No phosphazenium traces were detected in the ^{1}H NMR spectrum at 2.7 ppm (Fig. 2b'). The experimental molar mass was determined by ^{1}H NMR ($M_{n(NMR)}$) by comparing the signal integration of the initiator methylene group at 4.53 ppm with that of the methyl group in the repeating unit at 0.91 ppm. An M_n of 6100 g mol^{-1} was obtained, which is in very good agreement with the theoretical value ($M_{n(theo)}$ = 6400 g mol^{-1}). The PBO was then characterized by SEC using PMMA standards. The resulting SEC trace is monomodal with a low dispersity of 1.07 (Fig. 2d). $M_{n(SEC)}$ is slightly higher than $M_{n(theo)}$, but this difference can be attributed to the use of a PMMA standard. DSC analysis indicates that the PBOs are amorphous, with a T_g at -71 °C (Fig. 2e), which is consistent with previously reported values.[20] The T_g of PBO being lower than room temperature and the polymer being atactic, thus lacking a crystalline melting point, results in PBO being in a liquid state at room temperature. This property is particularly relevant for applications requiring increased molecular mobility, such as film formation or the encapsulation of hydrophobic active ingredients in nanoparticles. The lack of crystallinity, combined with a low T_g, also

improves miscibility with other organic compounds and can be adapted to its formulation by nanoprecipitation.

We next investigated PBO's behavior during nanoprecipitation given its defined molecular structure and thermophysical profile. We started with bulk methods to establish a comparative baseline.

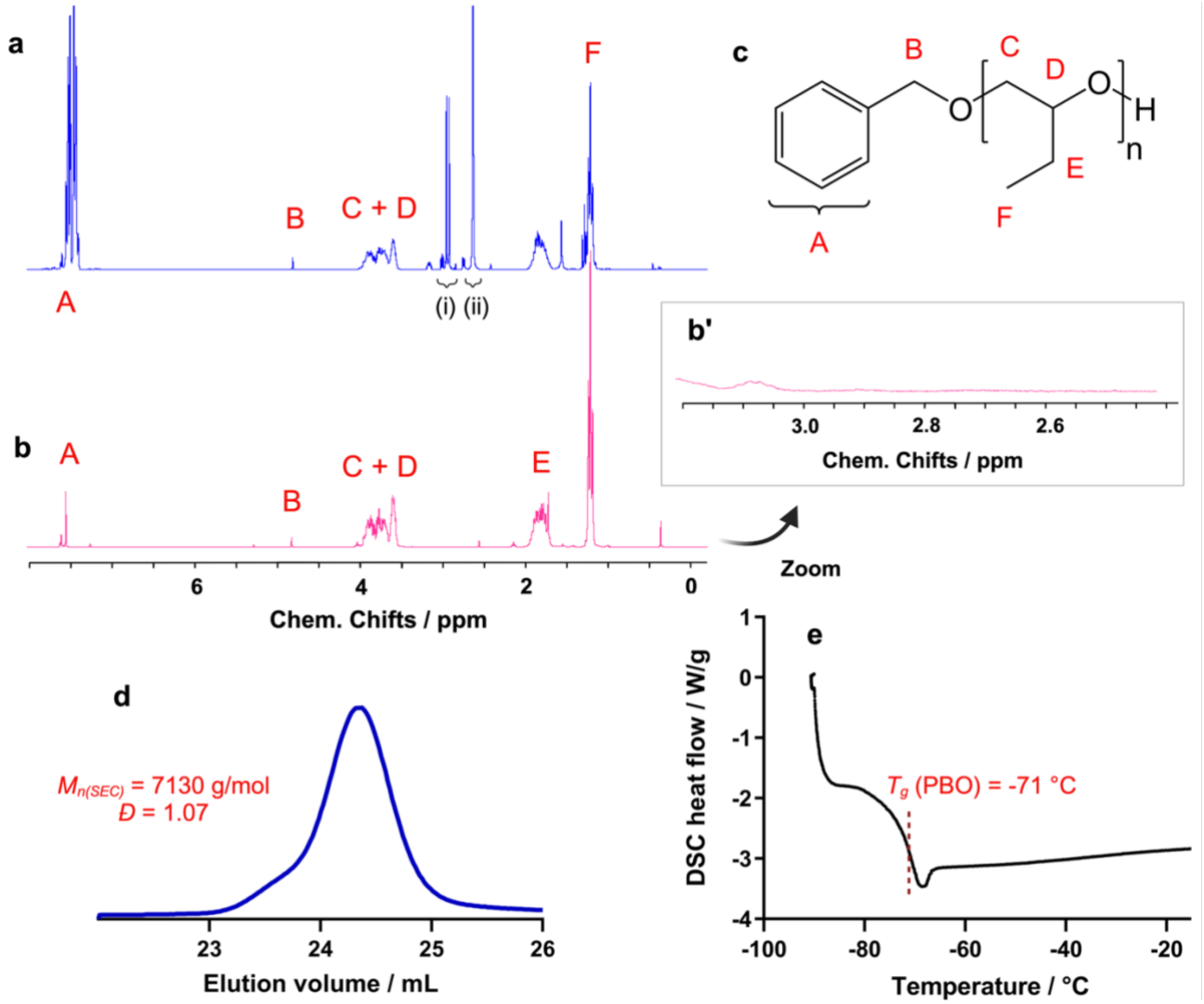

Fig. 2. Chemical characterization of PBO. NMR ^{1}H ($CDCl_3$, 298 K, 300 MHz, 64 scans) of PBO before treatment with alumina (a) and after treatment with alumina (b). In (b') a magnification of (b) spectrum. The chemical structure of PBO and corresponding NMR peaks are given in (c). In (d) SEC (in tetrahydrofuran) of PBO (PMMA standard), and in (e) DSC of PBO showing a glass transition temperature (T_g) at -71 °C. $M_{n(theo)}$ = 6400 g mol^{-1}, $M_{n(NMR)}$ = 6100 g mol^{-1}, $M_{n(SEC)}$ = 7130 g mol^{-1}. The polydispersity index ($Đ$) determined by SEC was 1.07. The peaks in (i) and (ii) correspond to phosphazene and toluene, respectively.

3.2. Design of PBO nanoparticles via bulk nanoprecipitation

After characterizing PBO's chemical properties, its apparent solubility in ethanol and in water was evaluated. PBO was found to be insoluble in water, though it was soluble in ethanol at a concentration of 7.5 mg mL^{-1}. In addition, PBO was found to be insoluble in a 1:2 v/v ethanol/water mixture, which is necessary to induce polymer precipitation.

To achieve smaller nanoparticle sizes, the PBO molar mass was kept below 10,000 g mol^{-1}, as higher molar masses of hydrophobic polymers are associated with larger nanoparticle sizes and increased aggregation.[7] Rapid mixing of the organic and aqueous phases was implemented to enhance solvent-water interdiffusion, which is critical for reducing nanoparticle size. The organic phase was thus rapidly injected into the aqueous phase with a syringe rather than added dropwise to ensure optimal mixing conditions. Specifically, 1 mL of the organic phase was injected within 4 seconds to ensure rapid and uniform dispersion.

DLS analysis of the nanoparticle suspension revealed a heterogeneous size distribution ranging from 80 to 255 nm (Fig. 3a). The *z*-average calculated from three independent experiments was 176 ± 7 nm, with a polydispersity index (PDI) of 0.142, indicating relatively low polydispersity.

Transmission electron microscopy images confirmed these results by showing nanoparticle sizes consistent with the DLS data (Fig. 3b-d). The smallest and largest observed nanoparticle sizes were 60 and 250 nm, respectively (indicated by green and red arrows in Fig. 3b(i) and Fig. 3c(ii), respectively). However, some particles appeared to be adhered together and deformed (blue arrow in Fig. 3d(iii)). This aggregation could explain the appearance of a secondary population in the DLS analysis, with particle sizes ranging from 3000 to 5000 nm (black arrow in Fig. 3a). The heterogeneous nanoparticle size and aggregation are likely consequences of the mixing conditions inherent to bulk nanoprecipitation. Although the organic phase was rapidly injected into the aqueous phase, the continuously changing volume ratio and flow rate between the two phases during mixing likely contributed to the size variability and aggregation. To overcome the limitations of bulk mixing and

enable precise control over PBO nanoparticle formation, we turned to microfluidic-assisted nanoprecipitation using hydrodynamic flow-focusing devices.

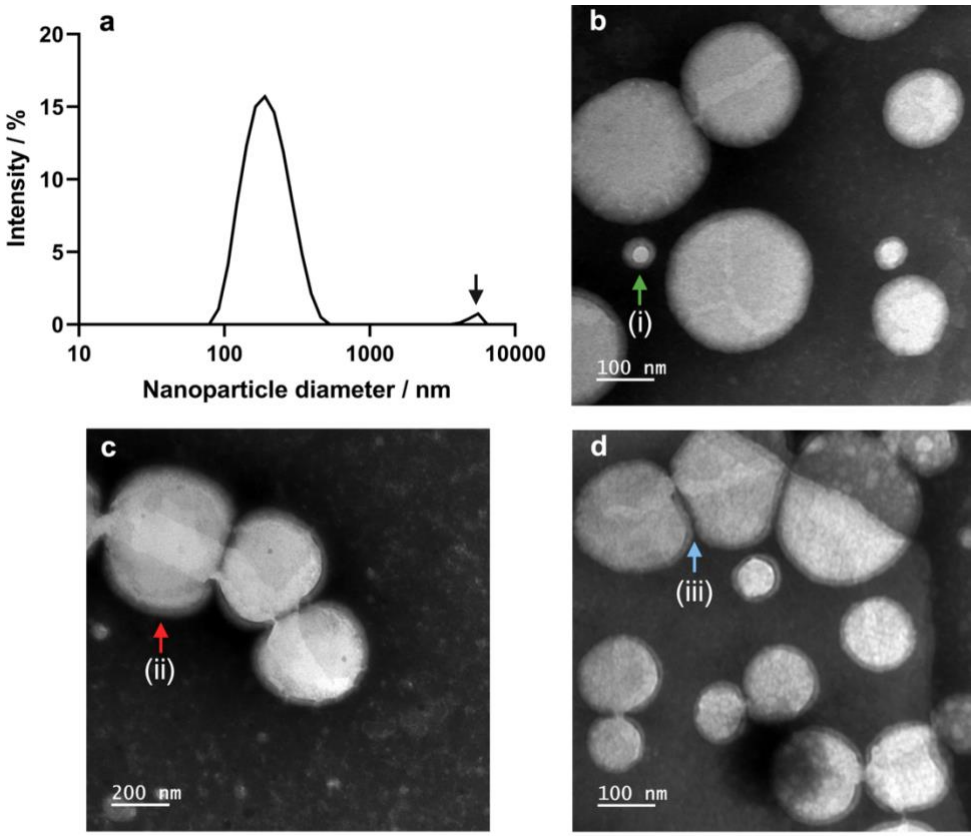

Fig. 3. Physicochemical characterization of PBO nanoparticles designed via bulk nanoprecipitation. The nanoparticle diameter in (a) was obtained by DLS. TEM images in (b), (c), and (d) were observed after adding a contrast agent. In (a), the black arrow corresponds to aggregates of PBO nanoparticles. The green (i) and red arrows (ii) indicated the smallest and the largest nanoparticles observed in TEM, respectively. The blue arrow (iii), highlights adhered or deformed nanoparticles.

3.3. Stepwise Optimization of Microfluidic Nanoprecipitation Conditions

3.3.1. Effect of PBO Concentration

We started the microfluidic optimization process by examining how the concentration of PBO in the organic phase influences nanoparticle formation, considering its direct impact on nucleation and growth kinetics. We designed PBO nanoparticles using a flow-focusing microfluidic device with a Ψ-geometry and channel dimensions of 100 × 100 μm. The flow ratio was maintained at 0.06, corresponding to an organic-to-aqueous phase ratio of 1:15. Lower flow ratio values are known to produce smaller nanoparticles.[14, 25] Experiments were conducted with three PBO concentrations of

7.5, 3.75, and 1.87 mg mL^{-1}. For each trial, the total flow was systematically increased from 32 to 96 µL min^{-1}, a threefold range.

As shown in Fig. 4a and 4b, there is a clear relationship between polymer concentration and nanoparticle characteristics. As the polymer concentration decreased, the mean hydrodynamic diameters and PDI of the nanoparticles consistently decreased as well, demonstrating the significant effect of polymer concentration on nanoparticle size (Fig. 4a(i) and 4b(iv)).

To further investigate this effect, nanoparticle size was analyzed at fixed total flow values (Fig. 4a(iii)). The results demonstrated a significant size reduction with decreasing PBO concentration. For example, at a total flow of 32 µL min^{-1}, the nanoparticle size decreased from 370 nm for 7.5 mg mL^{-1} to 173 nm for 1.87 mg mL^{-1} PBO concentration. These findings reinforce the critical influence of PBO polymer concentration on nanoparticle size under microfluidic conditions.

The impact of total flow on nanoparticle size was then assessed for each PBO concentration (Fig. 4a(ii)). Statistical analyses revealed no significant differences in nanoparticle diameter when total flow varied for a given concentration. A similar observation was made regarding the PDI variation shown in Fig. 4b(v). Although total flow influences the mixing rate, the results suggest that within the tested range, the mixing conditions were sufficient to ensure efficient solvent-water interdiffusion for each concentration.

In summary, in this first optimization section, we demonstrated the feasibility of designing PBO nanoparticles in a microfluidic device. In the next section, we investigated the effect of flow parameters on nanoparticle size and polydispersity. However, by decreasing the concentration of PBO from 7.5 mg mL^{-1} to 1.87 mg mL^{-1}, the mass of particles contained in the nanoparticle fraction further decreases by a factor of 8, lowering the mass yield of collected nanoparticles. In the next section, we investigated the impact of flow dynamics on nanoparticle size and dispersity.

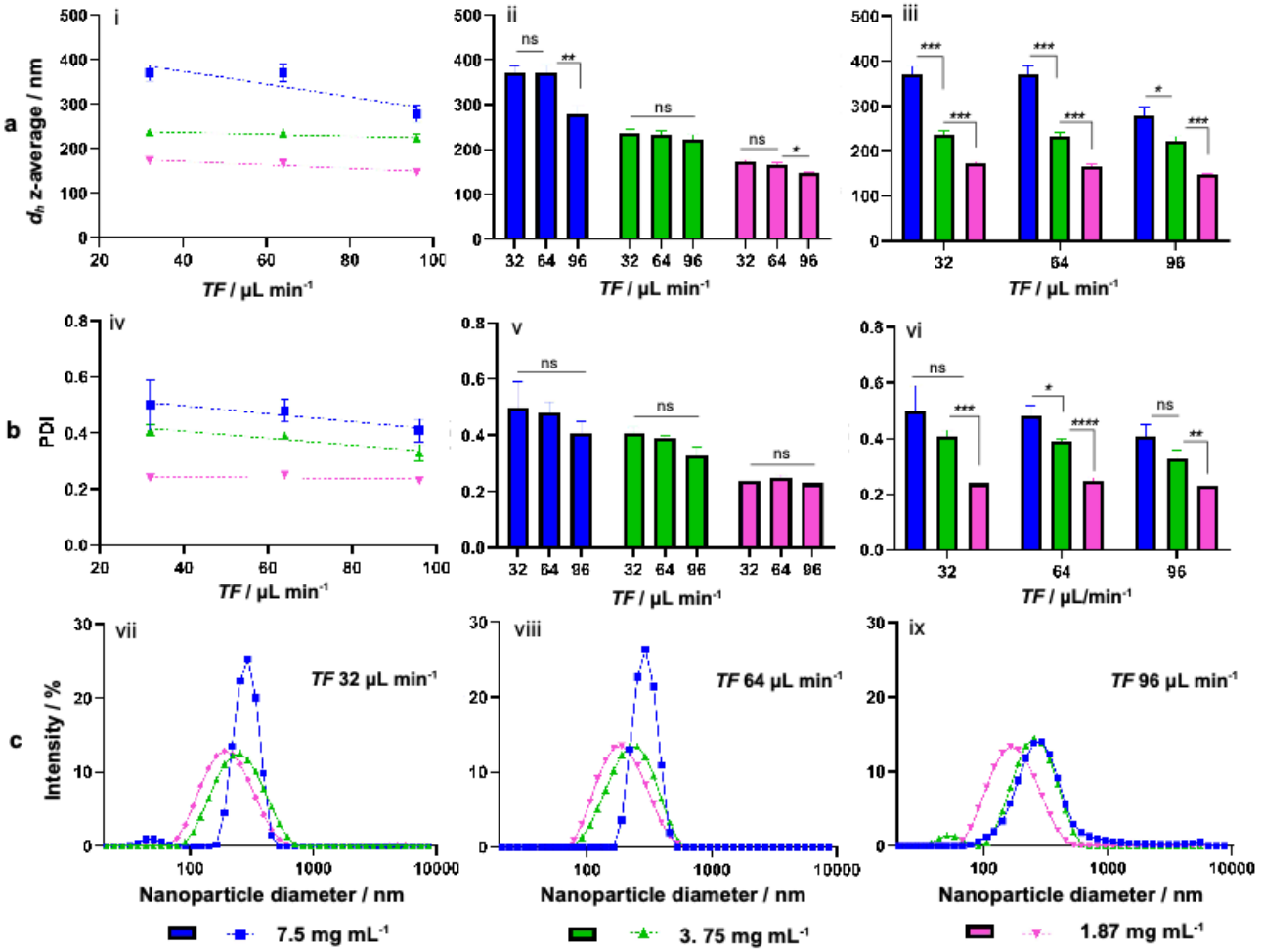

Fig. 4. Effect of PBO Concentration and total flow (*TF*) on Nanoparticle Size and PDI. (a) Mean hydrodynamic diameters (d_h) as a function of *TF*. (i) d_h values plotted on a consistent scale across *TF* values. (ii) Data presented to emphasize the effect of *TF* on d_h at each PBO concentration. (iii) Results plotted to highlight the effect of PBO concentration on d_h for each *TF* value. (b) Variations in PDI as a function of PBO concentration and *TF*. (iv) PDI values plotted versus *TF*. (v) Results highlighting the effect of *TF* on PDI at each PBO concentration. (vi) Data emphasizing the effect of PBO concentration on PDI at specific *TF* values. (c) Nanoparticle size distributions at *TF* values of 32 µL min^{-1} (vii), 64 µL min^{-1} (viii), and 96 µL min^{-1} (ix). PBO concentrations were 7.5 mg mL^{-1}, 3.75 mg mL^{-1}, and 1.87 mg mL^{-1} at a flow ratio (*R*) of 0.06 (1:15). Statistical analysis was performed with two-way ANOVA followed by Tukey's post-test. One, two, three, and four asterisks denote a *p*-value < 0.05, < 0.01, < 0.001, and <0.0001, respectively. "ns" denote a non-significant difference. Data represent mean values from three independent experiments (n = 3).

3.3.2. Influence of Flow Dynamics: Flow Ratio and Total Flow Rate

In this section, we evaluated the effects of flow dynamics—specifically, the flow rate ratio and the total flow—on nanoparticle size and polydispersity in Ψ-geometry microchannels. We varied the flow ratio between the organic and the aqueous phases from 0.1, 0.08, 0.06, and 0.05, which corresponded to the following ratios: 1:10, 1:12, 1:15, and 1:20. Our first observation of PBO nanoparticle size results in Fig. 5a,b and Table S4 is that variation in the flow ratio significantly affects the nanoparticle

size during the nanoprecipitation of PBO. A smaller flow ratio indicates a higher relative flow rate of the aqueous phase compared to the organic phase.

Small nanoparticles (203-242 nm) were obtained at low flow ratio values (R = 0.06 or 0.05), as reported in Fig. 5a,b, and detailed in Table S4. Large nanoparticles were obtained at high flow ratio values (0.1 and 0.08), corresponding to a higher organic phase flow compared to organic flow (306-380 nm) (Fig. 5a,b and Table S4). It is noteworthy that the mixing time decreased from approximately 7 to 2 ms as the flow ratio R decreased from 0.1 to 0.05 (Table S4).

In a second set of experiments, the total flow rate was modified for each flow rate ratio. Regardless of the flow rate ratio, increasing the total flow rate decreased the PBO nanoparticle size (Table S4) and Fig. 5a. The data shown in Fig. 4a and 4b are seen to be monotonically decreasing with a smaller decrease at higher total flow. We thus characterize the data with a power law of the form $d_h = A(TF)^{-\alpha}$, with the least-squares regression shown in Fig. S2. The best-fitting values are $A = 800 \pm 300$ nm $\left(\text{min } \mu\text{L}^{-1}\right)^{\alpha}$ and $\alpha = 0.3 \pm 0.1$. The errors represent a 95% confidence interval. As detailed in Table S4, the total flow is proportional to other relevant flow parameters, such as mixing speed (u_{mix}), and the Reynolds number (Fig. S3). These parameters were similarly characterized by the aforementioned power law above or other monotonically decreasing functions. Conversely, the total flow is inversely proportional to the residence time (τ_{Res} Eq. (D. 1), which is also proportional to the mixing distance (l_{mix} Eq. (E. 1). These parameters are therefore interdependent.

Together, these findings emphasize that microfluidic control of mixing speed, achieved through flow ratio and total flow rate, can be used to fine-tune nanoparticle size while maintaining formulation consistency. In the next section, we kept the flow ratio constant (R = 0.06) to understand the impact of total flow and channel geometry on PBO nanoparticle size, while varying the total flow, microfluidic geometry, and dimensions. This method yields different velocities for the same R.

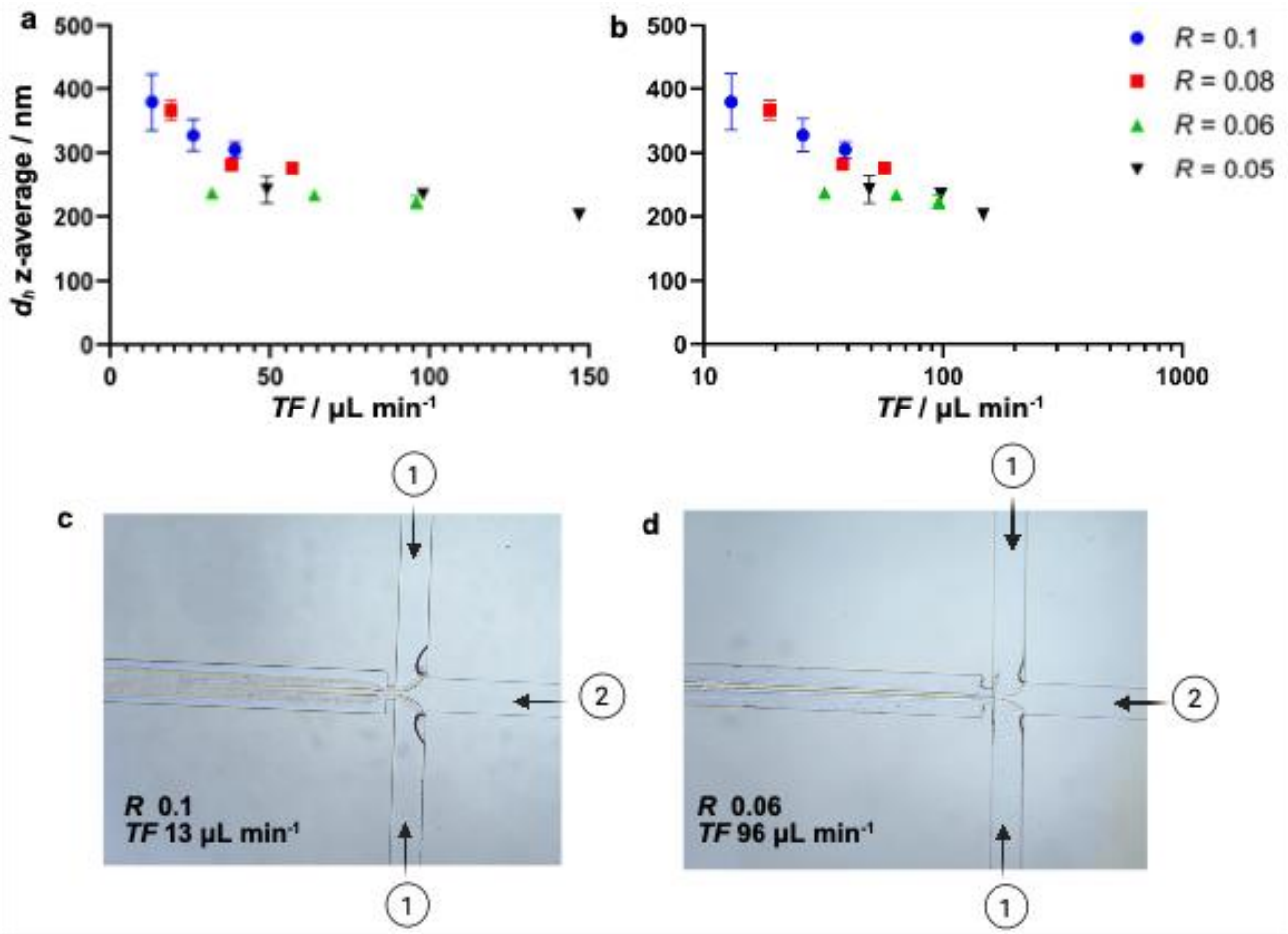

Fig. 5. Effect of total flow (*TF*) and flow ratio (*R*) on nanoparticle mean hydrodynamic diameters (d_h) for Ψ-geometry without junction. Nanoparticle size was plotted versus *TF* with a linear (a) and a logarithmic scale (b). *R* was changed as 0.1 (blue ●), 0.08 (red ■), 0.06 (green ▼), and 0.05 (black ▲), and the *TF* varies from 13 to 147 µL min^{-1}. (1) aqueous phase, (2) organic phase. Channel length l_1 was maintained at 10 mm. The PBO concentration was maintained at 3.75 mg mL^{-1}. Channels dimensions before mixing were w_3 = 75 µm and $h_{1\text{-}100}$ = 100 µm. Channels cross sections before mixing were $A_{B\text{-}100}$ = 7.5 × 10^3 µm^2. Channel dimensions after mixing were $W_{1\text{-}100}$ = 100 µm. Channel cross sections after mixing $A_{A\text{-}100}$ = 10^4 µm^2. (*n* = 3)

3.3.3. Impact of Microchannel Geometry and Dimensions

Lastly, we investigated how the physical design of the microfluidic device—namely channel geometry and cross-sectional dimensions—influences nanoparticle size and dispersity. In microfluidic-assisted nanoprecipitation, hydrodynamic flow-focusing (Ψ-geometry) is the most commonly reported mixing strategy. In contrast, T-mixing—initially used for optimizing nanoprecipitation parameters—has been investigated less frequently. To evaluate the influence of channel geometry on nanoparticle size and polydispersity index (PDI), we first modified the device design from a Ψ-geometry to a T-geometry. For each geometry, we systematically varied the channel dimensions and recorded the results, as summarized in Fig. 6 and Table S5.

In the T-geometry, the organic and aqueous phases are introduced from opposite sides of the channel and intersect at the mixing junction. Here, nanoparticle formation depends on the diffusion of solute molecules through the interdiffusion zone at the mixing point (denoted as "*z*" in Fig. 1c).[19, 26] For the largest channel dimension (100 × 100 μm), the resulting nanoparticles were consistently larger (>350 nm) as compared to those in similar Ψ-geometries, independent of the total flow rate (Fig. 6a, Table S5). The limited efficiency of molecular diffusion and heterogeneous local mixing conditions likely contributed to the larger nanoparticle sizes and broader size distribution. Decreasing the channel size from 100 μm to 40 μm did not significantly reduce nanoparticle size or PDI (Fig. 6 and Table S2). The larger PDIs observed in these channels can be attributed to inconsistent local mixing, resulting in uneven nucleation and growth dynamics. For the smallest channels (20 μm), nanoparticle sizes decreased significantly (188–202 nm) at low flow rates (2–4 μL min^{-1}) and low Reynolds numbers (*Re* = 10–21). At these scales, laminar flow dominates, making molecular diffusion the primary mixing mechanism. The reduced interphase diffusion distance enhances solvent-water interdiffusion and promotes smaller nanoparticle formation. However, operating at high flow rates in such small channels was challenging. Achieving optimal flow rates to balance nucleation and growth dynamics is essential for size uniformity.

In the Ψ-geometry, the organic phase flows through a central channel and is compressed symmetrically by the aqueous phase from two lateral channels, creating a narrowly focused stream. The focused organic stream minimizes diffusion distances, allowing for rapid and efficient solvent-water interdiffusion. In particular, for identical total flow and *R*, the Ψ-geometry contains a central wall that confines the organic phase. Furthermore, the square channel cross sections used here result in a different hydrodynamic context for the T- and Ψ-geometries, modifying any influence of shear between them. Based on our observations, we hypothesize that these differing contexts promote uniform nucleation in the Ψ-geometry and limit particle growth. This leads to smaller nanoparticles with narrower size distributions. The geometry facilitates rapid mixing at high speeds and effectively

displaces the organic solvent, which is crucial for forming small and uniform nanoparticles. Compared to other geometries, such as zig-zag and 3D architectures, which enhance mixing via chaotic advection, our Ψ-geometry offers enhanced control under laminar conditions and facilitates precise flow-focusing, especially at low Reynolds numbers. It is simpler and more reproducible to fabricate than 3D structures, making it favorable for scalable production. Symmetrical compression ensures uniform hydrodynamic focusing, which minimizes mixing heterogeneity and results in lower PDIs. Experimental results confirmed that the Ψ-geometry consistently produced smaller nanoparticles with narrower size distributions compared to the T-geometry, particularly at high flow rates. This is due to the improved mixing efficiency and controlled nucleation environment provided by hydrodynamic focusing.

The performance of Ψ_J-type geometries—where a junction is introduced upstream of the focusing region—was also evaluated. Importantly, the ratio between the junction width (w_2) and the main channel width (w_1) was kept constant at $w_2/w_1 = 5$ across all Ψ_J configurations to maintain geometric consistency. Despite this, the addition of the junction produced varied effects on nanoparticle size and stability, depending on the absolute channel dimensions. In the Ψ_J-100 × 100 μm configuration, particles were formed but were significantly larger than those formed in the Ψ-type geometry, indicating that the junction introduced unfavorable flow conditions that reduced mixing efficiency. In the Ψ_J-40×40 μm channels, no reliable size measurements could be obtained. Although DLS measurements yielded occasional particle size values, the count rate was unstable and highly variable across replicates, falling outside the optimal operating window (200–300 kcps) and dropping below 150 kcps (Table S6). This instability, combined with poor reproducibility, suggests that the nanoparticles were not colloidally stable and may have undergone rapid aggregation or phase separation after exiting the channel.

These effects cannot be explained by differences in the w_2/w_1 ratio, which was constant. Instead, we attribute the performance gap to the hydrodynamic disruption introduced by the junction itself. The

presence of the junction alters the flow profile just before the focusing region—creating recirculation zones, local shear gradients, and pressure variations—that interfere with the uniform convergence of the aqueous and organic phases.

This disruptive effect becomes more pronounced under high total flow rates. Both the Ψ_J-100 and Ψ_J-40 geometries were operated at relatively high TFs, corresponding to a moderate-to-high Reynolds number (Table S6). Under these conditions, the junction likely induces strong shear gradients and local pressure fluctuations that destabilize the focused stream, impairing mixing and increasing particle size. Furthermore, higher velocities reduce residence time in the mixing zone, limiting the extent of solvent–antisolvent interdiffusion and favoring aggregation.

By contrast, the Ψ_J-20 × 20 μm geometry produced stable nanoparticles, despite the presence of the same junction layout and the same w_2/w_1 ratio. A key difference lies in the flow regime: the Ψ_J-20 device was operated at significantly lower total flow rates, resulting in much lower Reynolds numbers. This promotes stable laminar flow and minimizes inertial effects at the junction, allowing solvent displacement and polymer precipitation to occur in a more controlled fashion. We hypothesize that this low-Re environment compensates for the presence of the junction by preserving the integrity of the focused stream and maintaining a favorable mixing.

These results collectively indicate that even with consistent geometric ratios, the impact of the junction is strongly dependent on flow conditions. High TFs and elevated Re in larger channels amplify flow asymmetry and destabilize the system, while low TFs in small channels maintain mixing control. Thus, both channel geometry and hydrodynamic regime must be co-optimized for stable nanoprecipitation of sensitive polymers like PBO.

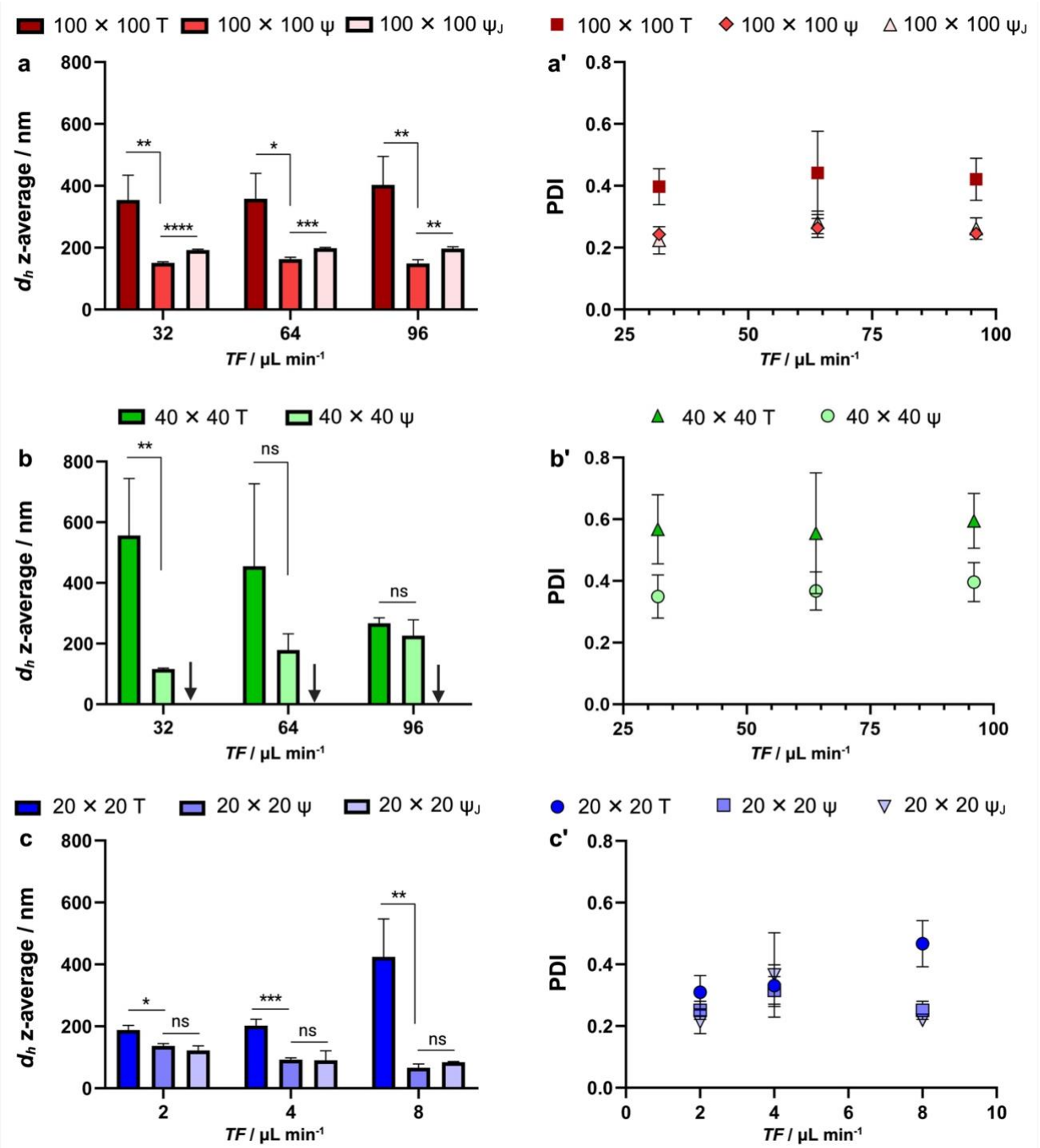

Fig. 6. Effect of channel geometry and total flow (*TF*) on mean hydrodynamic diameter (d_h) (a,b,c) and polydispersity (a',b',c') of PBO nanoparticles. (a,a') 100 × 100, (b,b') 40 × 40, (c,c') 20 × 20. In (b), black arrows refer to unstable nanoparticles obtained with the 40 × 40 geometry with a junction. The flow ratio *R* was maintained at 0.06. The PBO concentration was 1.87 mg mL^{-1}. Statistical analysis was performed with two-way ANOVA followed by Tukey's post-test. One, two, three, and four asterisks denote a *p*-value < 0.05, < 0.01, < 0.001, and <0.0001, respectively. "ns" denotes a non-significant difference.

4. Discussion

PBO presents unique formulation challenges due to its hydrophobicity and exceptionally low glass transition temperature (T_g = –71 °C). These characteristics have historically hindered the production of pure PBO nanoparticles for drug delivery applications, particularly those below 100 nm—a size range that is preferred for enhanced cellular uptake, improved tissue penetration, extended circulation time in the blood, and oriented biodistribution.[27, 28] Consequently, PBO has predominantly been used in block copolymers or blends rather than as a standalone material. Here, we report the first successful formulation of sub-100 nm pure PBO nanoparticles using microfluidic-assisted nanoprecipitation. This method achieves narrow size distributions without the need for structural modifications or copolymers. It is noteworthy that, while formulation parameters such as surfactant concentration can influence nucleation kinetics and colloidal stability, we deliberately fixed surfactant levels in this study. This ensured that the differences observed in nanoparticle size and polydispersity could be attributed solely to polymer concentration and hydrodynamic flow conditions.

Our results demonstrate that both PBO concentration and flow conditions significantly impact nanoparticle size and polydispersity. These findings align with established models of nanoprecipitation in microfluidic systems, which describe nanoparticle formation as a three-step process. When the PBO-containing organic phase is rapidly mixed with the water phase, the PBO's solubility decreases sharply, triggering the formation of initial nuclei. These nuclei grow by the further association of polymer chains until a steric barrier hinders further growth, resulting in kinetically trapped nanoparticles. The final particle size and uniformity depend heavily on the interplay between the mixing time and the aggregation time. The interplay between mixing time (τ_{mix}) and aggregation time (τ_{agg}) is critical to the outcome of nanoprecipitation. When $\tau_{mix} < \tau_{agg}$, mixing is effectively complete before aggregation begins, resulting in smaller, more uniform nanoparticles. In contrast, when $\tau_{mix} > \tau_{agg}$, aggregation occurs during incomplete mixing, leading to larger particle sizes and greater heterogeneity.

Due to its high molecular weight and hydrophobic nature, the diffusivity of PBO in aqueous systems is considerably lower than that of small molecules like ethanol. While ethanol diffuses in water at approximately 1.22×10^{-9} m^2 s^{-1}, the diffusivity of PBO is estimated at around 1×10^{-11} m^2 s^{-1}—consistent with values reported for other hydrophobic polymers undergoing nanoprecipitation in water-rich media.[23] Using a representative PBO concentration of 7.5 mg mL^{-1} (1.23 mol m^{-3} for M_n ≈ 6100 g mol^{-1}), and assuming nuclei radii of 5–10 nm,[14, 23] the estimated aggregation time ranged between 8 and 13 milliseconds (Table S7). Across all experimental conditions, our microfluidic device achieved mixing times from 0.1 to 7.5 milliseconds (Tables S3 and S4), satisfying the condition $\tau_{mix} < \tau_{agg}$ and supporting controlled nucleation over uncontrolled growth.

Polymer concentration significantly affected particle formation. Higher PBO concentrations increase the number of free unimers available to aggregate, resulting in more frequent collisions and the formation of larger, more polydisperse particles. At lower concentrations, aggregation is limited, producing smaller, more homogeneous nanoparticles (Fig. 4). Unlike amphiphilic block copolymers, which often yield small particles at high concentrations,[14, 29] pure PBO achieved the smallest size and greatest uniformity at lower concentrations (e.g., 1.87 mg mL^{-1}). However, this came at the cost of mass yield, emphasizing the need for an optimized balance. To achieve this balance, we selected an intermediate concentration of 3.75 mg mL^{-1} for further studies, allowing for controlled size reduction while maintaining practical throughput.

Beyond concentration, flow parameters—specifically total flow rate and flow ratio of the organic to the aqueous phases (R)—were found to play a critical role by altering the mixing efficiency within the microfluidic chip. At low flow ratios (*e.g.*, $R = 0.05$), the aqueous phase dominates and exerts high shear forces and compressing the organic stream into a narrow, diffusion-efficient profile. This promotes rapid solvent exchange and favors nucleation over growth, leading to smaller PBO nanoparticles. In contrast, increasing the flow ratio thickens the organic stream, reducing the surface-

to-volume ratio and slowing ethanol diffusion. This extends τ_{mix}, resulting in larger and more heterogeneous particles.

This behavior can be attributed to the Ψ-geometry of the microfluidic hydrodynamic flow-focusing device. At low flow ratios, the inner organic stream becomes thinner, enhancing interfacial mixing due to a higher surface-to-volume ratio. Conversely, high flow ratios produce thicker organic streams with slower mixing, which supports continued growth and aggregation. As shown in Fig.5c–d, thinner streams also result in a smaller volume of nucleating particles present at any given time. This reduces the probability of inter-particle collisions and further limits aggregation. Along with the flow ratio, the total flow rate is a complementary parameter that further modulates mixing efficiency and particle formation. The flow ratio primarily alters the width and geometry of the focused stream, while the total flow rate governs the overall velocity of the fluids and the strength of convective mixing. It is essential to understand how these two parameters interact because they jointly influence solvent exchange dynamics, nucleation timing, and the extent of polymer aggregation. We suggest that the correct theoretical context for these considerations is a system of advection-diffusion equations[30] for each of the three species. Notably, these equations should contain free energies of the Flory-Huggins type[31] with gradient terms,[32, 33] velocity profiles reminiscent of the flow junction, and the typical diffusive terms. The stability of concentration fluctuations and growth rates of metastable, phase-separating states[34] should then be investigated. Since the purpose of this article is not to address these theoretical questions in any detail, the following paragraphs empirically explore how variations in total flow rate, independent of flow ratio, impact nanoparticle size and uniformity by accelerating or constraining interfacial mixing further. We hope our observations will influence and inform later theoretical modelling.

At low total flow rates, the mixing of the organic and aqueous phases is primarily governed by molecular diffusion, resulting in slower interfacial exchange. The prolonged mixing time enables PBO polymer chains to aggregate more extensively before nucleation is complete, leading to the formation

of larger nanoparticles. As the total flow rate increases, convective forces enhance the mixing dynamics by compressing the focused stream. This accelerates solvent–water interdiffusion. Under these conditions, nucleation is favored over growth, producing smaller nanoparticles across all flow ratios (Table S2, Fig. 5a). This trend is less pronounced at the lowest flow ratios, as seen in Fig. 4, but becomes more evident under higher flow conditions, especially at elevated flow ratios (Fig. 5).

A power-law relationship was observed between total flow rate and nanoparticle diameter, indicating a scalable and predictable process–structure correlation. Total flow influences the Reynolds number, which affects mixing efficiency, interfacial mass transfer, and, ultimately, particle size. Although previous studies have demonstrated that turbulent mixing at high *Re* can facilitate efficient nanoprecipitation,[9, 10] the flow in our system remains in the laminar regime (Table S4), wherein mixing is primarily driven by diffusion and interfacial shear rather than turbulence.

Despite this laminarity, increasing the total flow rate enhances the convective contribution to mixing and reduces the mixing time. This favors earlier nucleation and limits particle growth and aggregation. Consequently, nanoparticle size decreases and becomes more uniform. However, very high total flow rates also reduce residence time within the microfluidic channel. When residence time approaches or falls below the time needed for molecules to diffuse across the focused stream, the extent of polymer precipitation may be limited, which can negatively impact nanoparticle uniformity. Karnik *et al*.[14] suggested that optimal nanoparticle formation requires the residence time to be greater than τ_{mix} but shorter than the overall aggregation time. The plateau in nanoparticle size observed at high total flows (Fig. 5a) likely corresponds to this window. At this point, the extent of aggregation has stabilized, and further increases in flow no longer influence particle size. Interestingly, variations in total flow had minimal impact on the polydispersity index of the resulting suspensions. This suggests that, although particle size is sensitive to hydrodynamic conditions, size uniformity is maintained over a broad range of flow rates.

Device geometry also significantly influenced nanoparticle characteristics. The Ψ-geometry produced smaller, more monodisperse PBO nanoparticles than the T-junction across various flow conditions and channel dimensions. This can be attributed to the more efficient hydrodynamic flow focusing enabled by Ψ-geometry, in which the organic stream is squeezed symmetrically between two aqueous streams. This configuration reduces diffusion distances, enhances interfacial contact, and improves solvent exchange. In contrast, the asymmetric flow profile of the T-junction appears less effective, especially for hydrophobic polymers like PBO that are susceptible to premature aggregation under suboptimal mixing conditions. Notably, the Ψ-geometry with narrow 20 μm channels produced the smallest reported PBO nanoparticles to date, down to 66 nm.

Moreover, the data presented in Fig. 6 highlight the critical role of microchannel geometry and total flow rate not only in determining nanoparticle size but also in modulating the PDI. In general, Ψ-geometries produced nanoparticles with consistently lower PDI values across all flow rates and channel dimensions compared to T- or Ψ_J-geometries. This suggests more homogeneous nucleation and growth in Ψ-type designs, likely due to their more symmetric and controlled hydrodynamic flow-focusing. In contrast, the introduction of a junction, as seen in Ψ_J geometries, induced broader size distributions—particularly in larger channels—due to unstable flow profiles and local mixing heterogeneities. Interestingly, narrowing the channels to 20 μm restored stability in Ψ_J devices and improved PDI, indicating that reduced diffusion lengths at low Reynolds numbers can offset geometric disruptions.

Overall, our results highlight how the design of microfluidic devices, combined with precise control of flow parameters, can overcome fundamental material limitations. While previous studies have examined flow and formulation parameters separately, our work integrates them through a unifying framework based on balancing mixing, nucleation, and aggregation timescales. Even under laminar flow, the geometry-driven enhancement of convective mixing mimics the benefits of turbulence, resulting in efficient nanoprecipitation and uniform particles. From a translational perspective, this

study provides practical guidance on formulating nanomedicines from highly hydrophobic or low-T_g polymers. Importantly, process optimization was achieved by maintaining a constant formulation while adjusting only the process parameters. This strategy could be advantageous for GMP-compliant scale-up and regulatory approval, as it avoids altering excipient compositions.

5. Conclusions

Microfluidic-assisted nanoprecipitation of hydrophobic polymers, such as PBO, provides a versatile and precise platform for designing nanoparticles with controlled size and uniformity. However, PBO's hydrophobicity and specific molecular characteristics require the careful optimization of process parameters to control the size and polydispersity of nanoparticles. Our study underscores the potential of microfluidic devices in overcoming these challenges. In PBO nanoprecipitation using flow-focusing Ψ-geometries, we found that lower flow rate ratios (organic:aqueous phases) generally produced smaller, more uniform nanoparticles due to enhanced solvent-water interdiffusion and rapid nucleation. In contrast, higher flow ratio values led to larger and more heterogeneous nanoparticles due to the longer diffusion times and prolonged growth phases. We also revealed that optimized total flow values are critical for achieving efficient mixing and precise nanoparticle formation. Higher total flow values improved mixing efficiency while maintaining laminar flow (*i.e.*, low to moderate Reynolds number), enabling consistent PBO nanoparticle synthesis. When the mixing geometry and channel dimensions were varied, we discovered that the Ψ-geometry demonstrated superior performance in producing small, uniform PBO nanoparticles through its confined flow-focusing. The T-geometry exhibited greater variability, likely due to an improved surface-to-volume ratio in the Ψ-geometry or different hydrodynamic contexts between the geometries. Reducing the channel dimensions, particularly to 20 μm, significantly improved nanoparticle size by shortening diffusion distances and enhancing mixing. However, incorporating mixing junctions did not improve size uniformity for the chips used here.

Future studies could focus on how PBO's hydrophobic nature interacts with various active ingredients, particularly poorly water-soluble drugs, during encapsulation to optimize drug-loading efficiency and release profiles. The insights gained from this study could also guide the nanoprecipitation of other hydrophobic polymers, thus broadening the applicability of microfluidic platforms to diverse materials and biomedical applications beyond PBO.

Author contributions

CT: writing – review & editing, funding acquisition, discussion

HK: Investigation and methodology for PBO synthesis and characterization and nanoparticle design in bulk nanoprecipitation.

JDM: conceptualization, supervision, writing – review & editing, methodology, funding acquisition, discussion

KB: conceptualization, project administration, supervision, investigation, writing - the first draft, writing – review & editing, methodology, funding acquisition, discussion, resources

LA: Investigation and methodology for nanoparticle design in microfluidic nanoprecipitation, formal analysis, discussion

MM: formal analysis, discussion

NI: Supervision of PBO synthesis and characterization, discussion

PG: Supervision of PBO synthesis and characterization, discussion

SHC: methodology and supervision for the preparation of microfluidic chips.

Conflicts of interest

There are no conflicts to declare.

Acknowledgments

Authors Kawthar Bouchemal, Nicolas Illy, and Philippe Guégan received funding from the ANR (ANR-21-CE09-0015). Author Kawthar Bouchemal received funding from the ANR (ANR-23-CE06-0019) and Chimie ParisTech, PSL University. Authors Kawthar Bouchemal, Christophe M. Thomas, and Joshua D. McGraw received funding from the Institut Pierre-Gilles de Gennes and PSL University. The present study has benefited from the core facilities of Imagerie-Gif, (http://www.i2bc.paris-saclay.fr), member of IBiSA (http://www.ibisa.net), supported by "France-Bioimaging" (ANR-10-INBS-04-01), and the Labex "Saclay Plant Science" (ANR-11-IDEX-0003-02), the Institut Pierre-Gilles de Gennes (Equipex ANR-10-EQPX-34 and Labex ANR-10-LABX- 31) and PSL Research

University (Idex ANR-10-IDEX-0001-02). The experimental work of this study also benefited from the technical contribution of the joint service unit CNRS UAR 3750 at the IPGG. No funders had any role in the study's design and data collection, analysis, and interpretation, nor in manuscript writing.

References

[1] M. Kuddushi, C. Kanike, B.B. Xu, X. Zhang, Invitation to submit to the Soft Matter 20th anniversary themed collection Recent Advances in Nanoprecipitation: From Mechanistic Insights to Applications in Nanomaterial Synthesis, Soft Matter (2025).
[2] H. Fessi, F. Puisieux, J.P. Devissaguet, N. Ammoury, S. Benita, Nanocapsule formation by interfacial polymer deposition following solvent displacement, International journal of pharmaceutics 55(1) (1989) R1-R4.
[3] D. Quintanar-Guerrero, E. Allémann, H. Fessi, E. Doelker, Preparation techniques and mechanisms of formation of biodegradable nanoparticles from preformed polymers, Drug development and industrial pharmacy 24(12) (1998) 1113-1128.
[4] J. Aubry, F. Ganachaud, J.-P. Cohen Addad, B. Cabane, Nanoprecipitation of polymethylmethacrylate by solvent shifting: 1. Boundaries, Langmuir 25(4) (2009) 1970-1979.
[5] K.H. Lee, F.N. Khan, I.B. Cosmin, D.U. Mualen, T.K. Porter, B.E. Wyslouzil, J.O. Winter, Semibatch and Continuous Electrohydrodynamic Mixing Nanoprecipitation for Scalable Polymer Nanostructure Production, ACS Applied Polymer Materials 6(20) (2024) 12382-12393.
[6] K. Bouchemal, S. Briançon, E. Perrier, H. Fessi, Nano-emulsion formulation using spontaneous emulsification: solvent, oil and surfactant optimisation, International Journal of Pharmaceutics 280(1-2) (2004) 241-251.
[7] P. Legrand, S. Lesieur, A. Bochot, R. Gref, W. Raatjes, G. Barratt, C. Vauthier, Influence of polymer behaviour in organic solution on the production of polylactide nanoparticles by nanoprecipitation, International journal of pharmaceutics 344(1-2) (2007) 33-43.
[8] S.A. Galindo-Rodríguez, F. Puel, S. Briançon, E. Allémann, E. Doelker, H. Fessi, Comparative scale-up of three methods for producing ibuprofen-loaded nanoparticles, European journal of pharmaceutical sciences 25(4-5) (2005) 357-367.
[9] K. Mitri, C. Vauthier, N. Huang, A. Menas, C. Ringard-Lefebvre, C. Anselmi, M. Stambouli, V. Rosilio, J.J. Vachon, K. Bouchemal, Scale-up of nanoemulsion produced by emulsification and solvent diffusion, Journal of Pharmaceutical Sciences 101(11) (2012) 4240-4247.
[10] M. Stumpo, C. Anselmi, C. Vauthier, K. Mitri, I. Hanno, N. Huang, K. Bouchemal, Scale-up of polyamide and polyester Parsol® MCX nanocapsules by interfacial polycondensation and solvent diffusion method, International Journal of Pharmaceutics 454(2) (2013) 678-685.
[11] A. Pietroiusti, L. Campagnolo, B. Fadeel, Interactions of engineered nanoparticles with organs protected by internal biological barriers, Small 9(9-10) (2013) 1557-1572.
[12] M.J. Mitchell, M.M. Billingsley, R.M. Haley, M.E. Wechsler, N.A. Peppas, R. Langer, Engineering precision nanoparticles for drug delivery, Nature Reviews Drug Discovery (2020) 1-24.
[13] T.M. Squires, S.R. Quake, Microfluidics: Fluid physics at the nanoliter scale, Reviews of Modern Physics 77(3) (2005) 977-1026. https://doi.org/10.1103/RevModPhys.77.977.
[14] R. Karnik, F. Gu, P. Basto, C. Cannizzaro, L. Dean, W. Kyei-Manu, R. Langer, O.C. Farokhzad, Microfluidic platform for controlled synthesis of polymeric nanoparticles, Nano letters 8(9) (2008) 2906-2912.
[15] T. Baby, Y. Liu, A.P. Middelberg, C.-X. Zhao, Fundamental studies on throughput capacities of hydrodynamic flow-focusing microfluidics for producing monodisperse polymer nanoparticles, Chemical Engineering Science 169 (2017) 128-139.
[16] R. Donno, A. Gennari, E. Lallana, J.M.R. De La Rosa, R. d'Arcy, K. Treacher, K. Hill, M. Ashford, N. Tirelli, Nanomanufacturing through microfluidic-assisted nanoprecipitation: Advanced analytics and structure-activity relationships, International Journal of Pharmaceutics 534(1-2) (2017) 97-107.
[17] Y. Bao, M. Maeki, A. Ishida, H. Tani, M. Tokeshi, Effect of organic solvents on a production of PLGA-Based drug-loaded nanoparticles using a microfluidic device, ACS omega 7(37) (2022) 33079-33086.
[18] J.-U. Joo, C.-H. Park, J. Yang, Y. Ko, S.S. Jee, H. Ahn, D.-P. Kim, Flash precipitation of random copolymers in a micro-mixer for controlling the size and surface charge of nanoparticles, RSC advances 14(27) (2024) 19147-19153.
[19] R.F. Ismagilov, A.D. Stroock, P.J. Kenis, G. Whitesides, H.A. Stone, Experimental and theoretical scaling laws for transverse diffusive broadening in two-phase laminar flows in microchannels, Applied Physics Letters 76(17) (2000) 2376-2378.
[20] R. Wehr, J. Gaitzsch, D. Daubian, C. Fodor, W. Meier, Deepening the insight into poly (butylene oxide)-block-poly (glycidol) synthesis and self-assemblies: micelles, worms and vesicles, RSC advances 10(38) (2020) 22701-22711.
[21] H. Du, F.A. de Oliveira, L.J.C. Albuquerque, G. Tresset, E. Pavlova, C. Huin, P. Guegan, F.C. Giacomelli, Polyglycidol-stabilized nanoparticles as a promising alternative to nanoparticle PEGylation: polymer synthesis and protein fouling considerations, Langmuir (2020).
[22] N. Illy, V. Corcé, J. Zimbron, V. Molinié, M. Labourel, G. Tresset, J. Degrouard, M. Salmain, P. Guégan, pH-Sensitive Poly (ethylene glycol)/Poly (ethoxyethyl glycidyl ether) Block Copolymers: Synthesis, Characterization, Encapsulation, and Delivery of a Hydrophobic Drug, Macromolecular Chemistry and Physics 220(16) (2019) 1900210.
[23] B.K. Johnson, R.K. Prud'homme, Mechanism for rapid self-assembly of block copolymer nanoparticles, Physical review letters 91(11) (2003) 118302.
[24] R. Diaz-Salmeron, C. Cailleau, S. Denis, G. Ponchel, K. Bouchemal, Hyaluronan nanoplatelets exert an intrinsic anti-inflammatory activity in a rat model of bladder painful syndrome/interstitial cystitis, Journal of Controlled Release 356 (2023) 434-447. https://doi.org/https://doi.org/10.1016/j.jconrel.2023.03.014.

[25] M. Abdelkarim, N.H. Abd Ellah, M. Elsabahy, M. Abdelgawad, S.A. Abouelmagd, Microchannel geometry vs flow parameters for controlling nanoprecipitation of polymeric nanoparticles, Colloids and Surfaces A: Physicochemical and Engineering Aspects 611 (2021) 125774.
[26] A.E. Kamholz, B.H. Weigl, B.A. Finlayson, P. Yager, Quantitative analysis of molecular interaction in a microfluidic channel: the T-sensor, Analytical chemistry 71(23) (1999) 5340-5347.
[27] J. Zhang, X. Ren, Z. Nie, Y. You, Y. Zhu, H. Chen, H. Yu, G.P. Mo, L. Su, Z. Peng, Dual-responsive renal injury cells targeting nanoparticles for vitamin E delivery to treat ischemia reperfusion-induced acute kidney injury, Journal of Nanobiotechnology 22(1) (2024) 626.
[28] Z.H. Mok, The effect of particle size on drug bioavailability in various parts of the body, Pharmaceutical Science Advances 2 (2024) 100031.
[29] W. Huang, C. Zhang, Tuning the size of poly (lactic-co-glycolic acid)(PLGA) nanoparticles fabricated by nanoprecipitation, Biotechnology journal 13(1) (2018) 1700203.
[30] B.J. Kirby, Micro-and nanoscale fluid mechanics: transport in microfluidic devices, Cambridge university press2010.
[31] A.J. Archer, B.D. Goddard, D.N. Sibley, J.T. Rawlings, R. Broadhurst, F.F. Ouali, D.J. Fairhurst, Experimental and theoretical bulk phase diagram and interfacial tension of ouzo, Soft Matter 20(30) (2024) 5889-5903.
[32] K. Roger, N. Shcherbakova, L. Raynal, Nanoprecipitation through solvent-shifting using rapid mixing: Dispelling the Ouzo boundary to reach large solute concentrations, Journal of Colloid and Interface Science 650 (2023) 2049-2055.
[33] C. Huang, M.O. de La Cruz, B. Swift, Phase separation of ternary mixtures: Symmetric polymer blends, Macromolecules 28(24) (1995) 7996-8005.
[34] A.J. Bray, Theory of phase ordering kinetics, Physica A: Statistical Mechanics and its Applications 194(1-4) (1993) 41-52.